

Generation of Mechanical Interference Fringes by Multi-Photon Quantum Measurement

M. Ringbauer,^{1,2} T. J. Weinhold,^{1,2} A. G. White,^{1,2} M. R. Vanner^{1,2,3,*}

¹*Centre for Engineered Quantum Systems,* ²*Centre for Quantum Computer and Communication Technology,
School of Mathematics and Physics, University of Queensland, Brisbane, QLD 4072, Australia,*

³*Clarendon Laboratory, Department of Physics, University of Oxford, OX1 3PU, United Kingdom*

The exploration of wave phenomena and quantum properties of massive systems offers an intriguing pathway to study the foundations of physics and to develop a suite of quantum-enhanced technologies. Here we present an optomechanical scheme to prepare non-Gaussian quantum states of motion of a mechanical resonator using photonic quantum measurements. Our method is capable of generating non-classical mechanical states without the need for strong single-photon coupling, and is resilient against optical loss and initial mechanical thermal occupation. Additionally, our approach provides a route to generate larger mechanical superposition states using effective interactions with multi-photon quantum states. We experimentally demonstrate this technique on a mechanical thermal state in the classical limit and observe interference fringes in the mechanical position distribution that show phase super-resolution. This opens a feasible route to explore and exploit quantum phenomena at a macroscopic scale.

INTRODUCTION

Generating quantum superposition states in macroscopic systems is an important goal in experimental quantum science. Studying such states will allow us to probe the limits of applicability of quantum mechanics and to harness quantum physics for new technologies. Early evidence for quantum phenomena with massive systems was provided by electron diffraction experiments [1] and, through the efforts of the last nine decades, quantum-matter-wave behaviour has been observed for neutrons [2], trapped ion systems [3], ultracold atoms [4], and even molecules comprising many hundreds of atoms [5]. A promising route to explore quantum behaviour on an even more macroscopic scale is provided by quantum optomechanics [6] where a mechanical oscillator interacts with an optical field via radiation pressure. This versatile quantum-optical platform enables tests of fundamental physics [7–9], the development of microwave-to-optical interfaces [10], and high-precision weak-force sensors [11]. Indeed, the LIGO gravitation-wave antenna can be considered a large-scale optomechanical system [12, 13]. Recently, impressive progress has been made using both opto- and electro-mechanical systems with examples including single-phonon-level operations [14–17], quantum coherent coupling [18], mechanically-induced squeezing of light [19, 20], and even opto-mechanical entanglement [21]. Experimental efforts continue in a diverse set of directions, however, progress is hindered by three main factors: weak single-photon coupling, sensitivity to optical loss, and mechanical decoherence. The approach we introduce here exploits measurement-induced non-linearities [22] to overcome the challenges of weak coupling and optical loss. In addition, our approach of-

fers resilience against initial thermal occupation and can also be readily employed in cryogenic systems to overcome the challenge of thermal decoherence.

To understand radiation pressure consider the reflection of a single photon from a mechanical resonator. The reflection imparts a momentum—inversely proportional to the wavelength—onto the resonator and concurrently the optical field acquires a phase-shift—proportional to the mechanical displacement. This momentum, however, is typically very small compared to the quantum noise of the resonator due to weak optomechanical coupling. In order to enhance the strength of this interaction, experimental efforts often employ an optical cavity to increase the number of reflections [6]. Utilising such cavity enhancement, the seminal works of Bose, Jacobs, and Knight [7]; and Marshall *et al.* [8], proposed using a superposition of the optical vacuum and a single photon to generate optomechanical entanglement with the motion of a mechanically oscillating mirror forming part of a Fabry-Perot cavity. In this case, the mechanical resonator is subject to a quantum superposition of the identity operation (no photon present) and a displacement operation (single photon present), thus generating a mechanical Schrödinger-cat state.

Our method enables the generation of mechanical superposition states without the need for non-classical optical input states such as single photons. Rather, we use an optomechanical interaction for a time much shorter than the mechanical period [23] with a weak optical coherent state and then project the reflected field, via photon counting, onto a superposition of zero and one photon to conditionally generate the superposition. In contrast to Refs. [7, 8], the measurement used in our scheme leaves the mechanics in a single-mode superposition state, which is achieved by projection from a more easily prepared form of optomechanical correlations. A single-mode quantum superposition state—with components separated in the momentum quadrature—will show

* Email correspondence: michael.vanner@physics.ox.ac.uk

interference fringes in the position probability distribution with a frequency inversely proportional to the superposition separation. When the photon detection registers the required event to prepare such a state an independent readout beam is then used to verify and characterise the mechanical state. The process of our scheme is non-classical and generates quantum states of motion independent of the coupling strength and for finite initial thermal occupation. Moreover, the size of the generated mechanical superposition state can be made larger by projection onto an optical $N00N$ -state [24–26], which can be implemented using coherent state inputs, multi-port interferometry, and multi-photon coincidence measurements [27]. Unlike preparation of large $N00N$ states, projection onto these states is experimentally simple. We implement this process experimentally and observe the first mechanical interference fringe pattern and the predicted phase-superresolution for a two-photon coincidence measurement. In this proof-of-concept experiment we observe a high-visibility fringe pattern in the mechanical position but we do not observe any non-classical features due to quantum decoherence and low readout sensitivity. Generating and observing single-mode non-classicality, such as Wigner negativity, of a massive mechanical oscillator remains an outstanding challenge. Our measurement-based-scheme offers a promising route to achieving this important goal and can be readily applied to a number of optomechanical systems beyond the system used here. This experimental technique provides a powerful platform to empirically explore open-quantum-system dynamics, test potential collapse models of the wavefunction [28–30], and enable the development of quantum-enhanced weak force sensors.

RESULTS

Mechanical state preparation via photon detection— For simplicity we first describe our scheme for two-port photon counting before generalizing to multi-port quantum measurement. The two-port case describes our experimental results and can be implemented with Mach-Zehnder-type interferometers. Figure 1A shows a conceptual model of our experiment, where a weak coherent state is injected and interacts with a mechanical resonator in one arm of an interferometer. The two optical fields inside the interferometer then interfere on a beam-splitter and photon counting is performed on the two output ports. A single-photon click on one of the detectors effectively projects the optical state that was inside the interferometer onto the path-entangled number state, i.e. $(|10\rangle + |01\rangle)/\sqrt{2}$, which is the state used in Refs. [7, 8]. If, instead, both detectors register a single photon then, due to second-order quantum interference, the optical state that interacted with the mechanical resonator within the interferometer must have been a 2-photon $N00N$ -state $(|20\rangle - |02\rangle)/\sqrt{2}$. In this case, the mechanical oscillator was subject to a superposition of the identity operation

and a two-photon radiation-pressure displacement, thus enhancing the size of the superposition by a factor of two compared with the single photon detection case.

This operation can be conveniently described using the measurement- (or Kraus-) operator approach, which allows us to conveniently compute the mechanical state after a measurement as well as the measurement outcome probabilities. Consider a mechanical resonator in the pure initial state $|\psi_{\text{in}}\rangle_{\text{M}}$ and coherent states $|\alpha\rangle_1|\alpha\rangle_2$ in the interferometer arms 1 and 2, respectively (i.e. the state after the initial 50/50 beamsplitter in Fig. 1A). The state immediately after the interaction with mode 1 of the interferometer is then given by $e^{i\mu a_1^\dagger a_1 X_{\text{M}}}|\alpha\rangle_1|\alpha\rangle_2|\psi_{\text{in}}\rangle_{\text{M}}$, where, $\mu = 4\pi x_0/\lambda$ is the momentum transfer per photon in units of the mechanical quantum noise. Here, $x_0 = \sqrt{\hbar/m\omega}$ is the mechanical ground state size (m ; effective mass, ω ; mechanical angular frequency), $X_{\text{M}} = x/x_0$ is the mechanical position operator in units of x_0 , and $a_{1,2}$ are the annihilation operators for the interferometer arms 1 and 2. The two optical fields then interfere on a beam-splitter, via $B^\dagger a_1 B = t a_1 + r a_2$ and $B^\dagger a_2 B = r a_1 - t a_2$, where r^2 and t^2 denote the intensity reflectivity and transmittivity, respectively. The mechanical state after this interaction and photon measurement is $|\psi_{\text{out}}\rangle_{\text{M}} \propto {}_2\langle n|_1\langle m|B e^{i\mu a_1^\dagger a_1 X_{\text{M}}}|\alpha\rangle_1|\alpha\rangle_2|\psi_{\text{in}}\rangle_{\text{M}}$, where m and n denote the number of photons detected in mode 1 and 2 after the beam-splitter, respectively. Assuming a 50:50 beam-splitter and including a static phase-shift ϕ in mode 2 of the interferometer we can introduce the measurement operator,

$$\Upsilon = \frac{e^{-|\alpha|^2}}{\sqrt{m!n!}} \frac{\alpha^{m+n}}{(\sqrt{2})^{m+n}} (e^{i\mu X_{\text{M}}} + e^{i\phi})^m (e^{i\mu X_{\text{M}}} - e^{i\phi})^n. \quad (1)$$

The mechanical output state can now be written $|\psi_{\text{out}}\rangle_{\text{M}} \propto \Upsilon|\psi_{\text{in}}\rangle_{\text{M}}$. This operation corresponds to a superposition of a mechanical displacement $e^{i\mu X_{\text{M}}}$ and the identity operation with a controllable phase $e^{i\phi}$. More generally we may compute the mechanical state via $\rho_{\text{M}}^{\text{out}} = \Upsilon \rho_{\text{M}}^{\text{in}} \Upsilon^\dagger / \mathcal{P}$, where $\rho_{\text{M}}^{\text{in},\text{out}}$ are the input and output mechanical density matrices, respectively, and $\mathcal{P} = \int_{-\infty}^{\infty} dX_{\text{M}} \Upsilon^\dagger \Upsilon \langle X_{\text{M}} | \rho_{\text{M}}^{\text{in}} | X_{\text{M}} \rangle$ is the probability for obtaining the photon counting outcomes m and n , see Supplementary Materials for further details.

To examine the mechanical position probability distribution of the state after the interaction and measurement we may write $\langle X_{\text{M}} | \rho_{\text{M}}^{\text{out}} | X_{\text{M}} \rangle \propto \Upsilon^\dagger \Upsilon \langle X_{\text{M}} | \rho_{\text{M}}^{\text{in}} | X_{\text{M}} \rangle$. The function $\Upsilon^\dagger \Upsilon$ is oscillatory in X_{M} , as obtaining a click in our interferometer gives periodic information about X_{M} , and can be interpreted as a filter acting on the initial mechanical position probability distribution. This oscillatory behaviour is intrinsically linked with the cubic nature of the full optomechanical radiation-pressure interaction $a_1^\dagger a_1 X_{\text{M}}$ and the non-linearity of photon counting. This allows our scheme to generate non-Gaussian states of motion, which would not be possible in the more commonly considered linearized regime with quadratic inter-

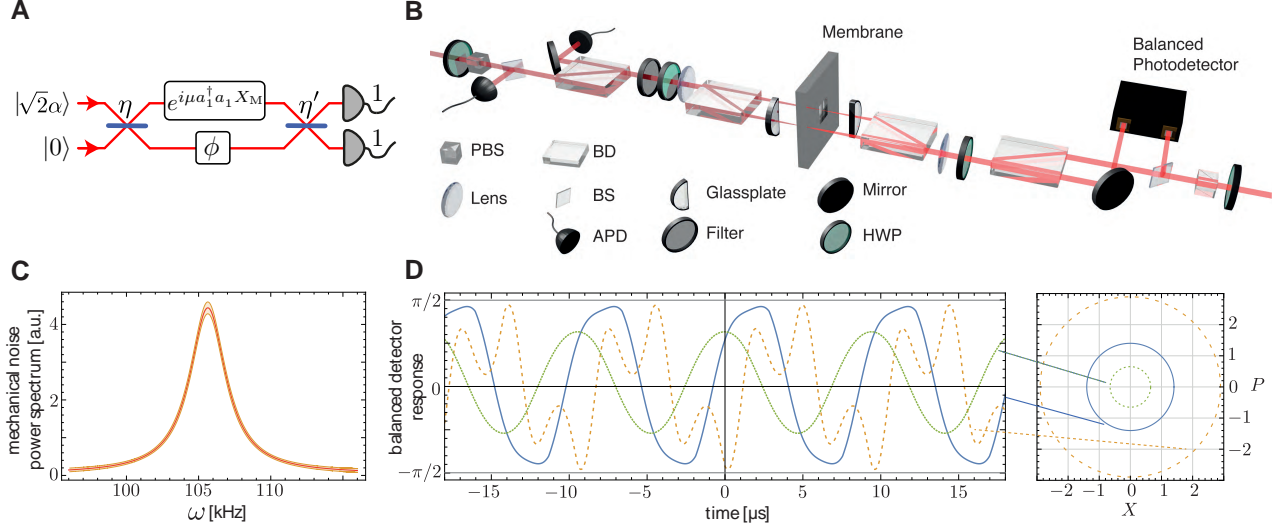


FIG. 1. Experimental scheme. (A) A mechanical resonator interacts with a weak optical coherent state inside an interferometer with static phase-shift ϕ formed by two beam splitters with reflectivities η and η' . The optomechanical radiation-pressure interaction is described via the unitary operation $e^{i\mu a_1^\dagger a_1 X_M}$, where a_1 describes the optical field operator, and X_M describes the mechanical position. Mechanical interference fringes are generated via photon counting on the two interferometer outputs, which projects the field inside the interferometer onto a path-entangled photon number state. (B) In our experiment the two interferometer paths in A are represented by orthogonal polarizations of a weak coherent-state, and a half-wave plate (HWP) acts as a tunable beam splitter. For the interaction with the mechanical resonator—a SiN membrane—the polarization modes are split into distinct optical paths using a calcite beam displacer (BD). One of the beams reflects off the membrane, while the other one reflects off the adjacent frame and acquires a static phase shift ϕ , controlled by the yaw degree of freedom of the BD. The modes are then interfered, separated, and detected by two single-photon detectors (APD). A position measurement of the membrane is performed from the other side of the membrane using a similar setup and an independent readout beam. Lenses focus the preparation and readout beams to a spot size of $\sim 50 \mu\text{m}$ on the membrane and glass plates are used to compensate for shifts in the foci due to the birefringence in the BDs. (C) Noise power spectrum of the fundamental vibrational drum mode of the mechanical resonator with resonance frequency of $\omega_M/2\pi = 105.64 \text{ kHz}$. (D) Balanced-detector time-traces used to measure the mechanical state for three example phase space points (shown on the right) with displacements of 103 nm (dotted, green), 222 nm (solid blue) and 458 nm (dashed, orange), respectively. Here X and P are the mechanical position and momentum quadratures, respectively, in units of the interferometer readout range $\lambda_r/4 = 158.2 \text{ nm}$ (corresponding to the turning-points of the interferometer).

actions and linear measurements.

Experimental Setup— In our experiment (Fig. 1B) we use a high-stress $1.7 \times 1.7 \text{ mm}$ Si_3N_4 membrane [32] embedded in a $10 \times 10 \text{ mm}$ Si-frame. The membrane has a thickness of $50 \pm 2.5 \text{ nm}$ and at our state-preparation-field wavelength of 795 nm has a measured reflectivity of $23.0 \pm 0.5 \%$, while the frame has a reflectivity of $20.5 \pm 0.2 \%$. The noise-power spectrum of the fundamental drum mode at $\omega_M/2\pi = 105.64 \pm 0.02 \text{ kHz}$ is shown in Fig. 1C. At room temperature and at atmospheric pressure the mechanical line-width (FWHM) was measured to be $\delta\omega_M/2\pi = 3.10 \pm 0.05 \text{ kHz}$ and the effective mass is on the order of 100 ng , which comprises approximately 10^{16} atoms. In order to probe the regime where the optomechanical phase shifts are large, i.e. $\mu^2 \langle X_M^2 \rangle \gtrsim 1$, we use a ring-piezo to drive the membrane motion.

The membrane is mounted in a way that allows optical access from both sides, and forms the central part of two folded Mach-Zehnder interferometers (MZI), see Fig. 1B. One interferometer is used for mechanical state prepara-

tion with photon counting, as illustrated in Fig. 1A, while the other is used for mechanical position readout using a balanced detector and a $\sim 100 \mu\text{W}$ laser at a wavelength of 632.8 nm . Our setup employs a compact polarization interferometer design that does not require active phase stabilisation [33]. The two arms of the MZI in Fig. 1A are represented by orthogonal polarizations and the role of the beamsplitter is achieved by a half-wave plate (HWP), which allows for precise control of the splitting ratio. For the interaction with the membrane the two polarizations are separated using a calcite beam-displacer and recombined after reflection from the mechanical device.

An APD click—either one of the detectors or a coincidence event within a 7.8 ns window—triggers the balanced detector and recording of a $50 \mu\text{s}$ long trace at a sampling rate of 100 MS/s , see Fig. 1D. The mechanical quadratures X and P , defined in units of the interferometer readout range ($\lambda_r/4$), are then extracted from a fit to this time trace. For small mechanical displacements the time trace is almost sinusoidal, but becomes

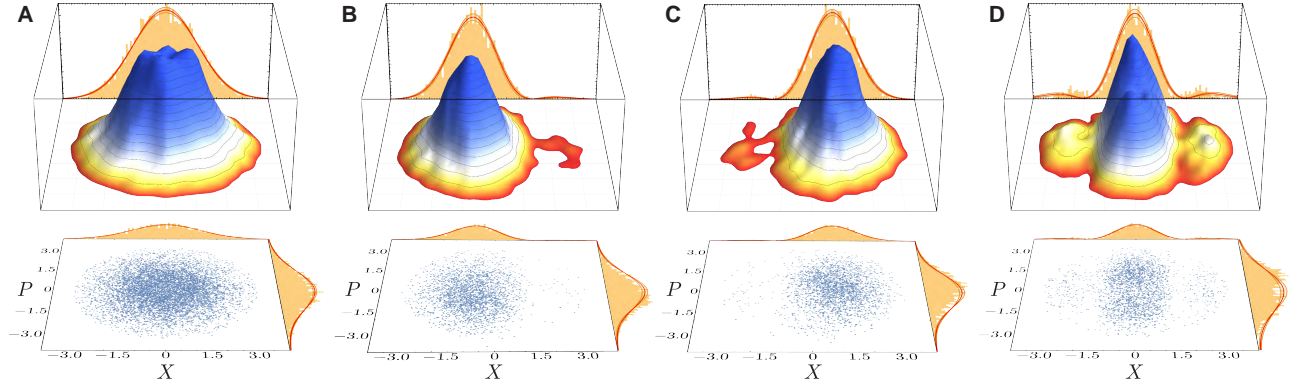


FIG. 2. Observed mechanical states of motion showing interference fringes. Each plot shows the measured phase-space points (bottom), together with the corresponding mechanical position and momentum quadrature histograms, and a normalized 3D probability-density histogram of these points (top), with the mechanical position quadrature histogram reproduced again for easy visualization. The quadrature histograms contain a fit (solid, red line) using the theory model and corresponding 3σ mean prediction bands (shaded orange). All axes are in units of the interferometer readout range. **(A)** Measured initial Gaussian thermal state. (The truncation at the origin is due to finite resolution of our data acquisition.) **(B)** Conditional motional state prepared via $\{m, n\} = \{0, 1\}$ detection, which is shifted in phase-space along $-X$ and shows the start of a second peak in the right tail of the Gaussian envelope. **(C)** Conditional state for $\{m, n\} = \{1, 0\}$ detection, which is as B, but shifted along $+X$. Again, note the second peak, now on the left. **(D)** Two photon ($\{m, n\} = \{1, 1\}$) detection generates a mechanical fringe pattern in X with twice the frequency of the single photon detection cases due to super-resolution of the measurement. Three maxima of the fringe pattern are observed. In all of these cases the interferometer phase ϕ was set to $\pi/2$. Also note that the momentum quadrature remains close to the initial distribution for all of these measurements.

overmodulated as the resonator displacement surpasses ~ 100 nm. In addition, for larger mechanical displacements we observe a mechanical-position-dependent amplitude modulation of the interferometer signal. We have taken the first order corrections due to this amplitude modulation into account when fitting the time traces, see Supplementary Material. For each type of click event we record ~ 3000 such time traces to create a phase-space histogram of the mechanical motion. By using a combination of spectral and polarization filters the read-out beam transmitted through the membrane is suppressed below the dark-count level of our single-photon detectors of ~ 150 Hz.

Large phase-shift regime— Figure 2 shows the measured mechanical phase-space distributions prepared via one- and two-photon measurements on a piezo-driven initial Gaussian thermal-state (Fig. 2A) with RMS position fluctuations of 198 ± 2 nm. This corresponds to the regime of large optical phase-shifts, i.e. $\mu^2 \langle X_M^2 \rangle \gtrsim 1$. For single-photon detection, low frequency fringes are observed with a π phase-shift between the detection events $\{m, n\} = \{0, 1\}$ (Fig. 2B) and $\{1, 0\}$ (Fig. 2C). Moreover, we observe the start of the second fringe peak in the tails of the Gaussian envelope, which is on the right in Fig. 2B and the left in Fig. 2C. In the case of a two-photon detection event $\{m, n\} = \{1, 1\}$ (Fig. 2D), the mechanical resonator interacted with an effective two-photon $N00N$ state. Consequently, we observe phase super-resolution in the mechanical interference pattern at twice the fringe-frequency of the single photon cases. We would like to highlight that this work goes significantly beyond previous all-optical schemes observing phase super-resolution

via multi-photon projection [27, 31] as our scheme maps the fringe pattern into the state of another *bosonic mode* rather than being a modulation to the photon count rate with a *scalar* phase quantity. Thus, the super-resolution achieved by such projections is used here as a resource for state preparation. In a quantum regime, the fringe pattern observed can then be interpreted as either the quantum interference in the superposition state or from the filter of the quantum measurement. This measurement-based technique provides a considerable advantage for ultimately generating non-classical states of mechanical motion and can be employed in other quantum optical systems. Note that all conditional states (Fig. 2B-D) feature interference fringes in the position distribution, while the momentum quadrature remains as the initial Gaussian distribution. The conditional mechanical states shown here were prepared with the phase set to $\phi = \pi/2$, which gives a fringe maxima in the centre of the distribution for the $\{1, 1\}$ event.

We would like to additionally note here that our method can be utilised to determine the optomechanical coupling strength μ by fitting to the fringe pattern observed. This technique requires a well calibrated position axis in units of the mechanical ground state size and can be performed for any mechanical thermal occupation.

Small phase-shift regime— Our scheme can also generate non-Gaussian states of motion in the regime of small optomechanical phase shifts, i.e. $\mu^2 \langle X_M^2 \rangle \ll 1$. Indeed, mechanical non-classicality, in the form of Wigner negativity, can be generated independent of the coupling strength, providing a promising route to generate and explore macroscopic mechanical quantum states even for

systems with weak single-photon-coupling. For small μ , applying our scheme to the mechanical ground state for $\{m, n\} = \{0, 1\}$ with $\phi = 0$ yields $(e^{i\mu X_M} - 1)|0\rangle \simeq (i\mu X_M)|0\rangle = i\mu 2^{-1/2}|1\rangle$. Here, $|1\rangle$ denotes a single phonon Fock state and the mechanical position operator in terms of the phonon annihilation (b) and creation (b^\dagger) operators is $X_M = 2^{-1/2}(b + b^\dagger)$. This conditional state is a result of quantum interference and has no classical description [34–36]. Note that in this regime the detection event $\{m, n\} = \{1, 1\}$ generates a similar state. The Wigner function of this mechanical single-phonon Fock state and its two conjugate quadrature distributions are shown in Fig. 3B. A mechanical Fock state has a rotationally invariant distribution in phase-space and has the quadrature distribution $\text{Pr}(X_M) = 2\pi^{-1/2} X_M^2 e^{-X_M^2}$ for all quadrature angles. For $\mu^2 \langle X_M^2 \rangle \ll 1$ the filter for these detection events is $\Upsilon^\dagger \Upsilon \propto \mu^2 X_M^2$. Thus, we note that the position probability distribution after this operation has the same form as a Fock state for any thermal occupation, not just the ground state.

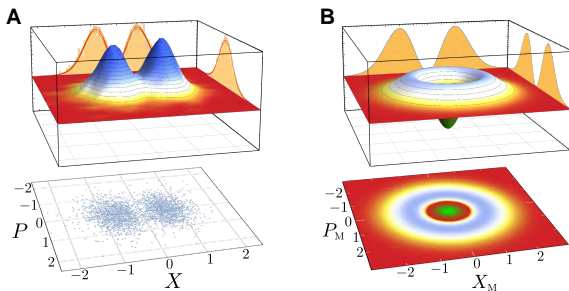


FIG. 3. Non-Gaussian mechanical states prepared with weak single-photon coupling. (A) Experimentally observed mechanical phase-space distribution for the detection event $\{m, n\} = \{1, 1\}$ with $\phi = 0$ in the weak coupling and weak drive regime, in units of the interferometer read-out range. The position probability distribution here has the same form as that of a single phonon Fock state. (B) Theoretical Wigner function of single phonon Fock state, plotted in units of the mechanical quantum noise. This state would be obtained when applying our scheme to the mechanical ground state for the same parameters as in Fig. A. Note that the Fock state has a non-Gaussian momentum distribution whereas our data has a Gaussian momentum distribution due to the thermal initial state.

To observe this type of fringe pattern we use the detection event $\{m, n\} = \{1, 1\}$ on a mechanical thermal state with RMS position fluctuations of 91 ± 1 nm. The observed mechanical phase-space distribution and quadrature distributions are shown in Fig. 3A. The measured position probability distribution is in good agreement with the theoretical prediction. Note that, for this large thermal excitation, however, the momentum quadrature probability distribution remains Gaussian.

Generalisation to larger N00N states— Our scheme can be extended to generate mechanical superposition states with increasing separation size by only changing

the optical measurement. This extension would require two coherent states, one of which interacts with the mechanical system, while the other acquires a static phase shift, together with $N - 2$ vacuum ancilla modes injected into an optical N -port interferometer, see Fig. 4A. N -fold single-photon detection at the output of the N -port then projects the optical field so that the mechanical resonator effectively interacted with an optical $N00N$ -state. The mechanical resonator is thus subject to a superposition of a radiation-pressure force with 0 or N photons thus enhancing the separation in the superposition state (cf. Fig. 4B). See the Supplementary Material for a mathematical description and the heralding probability. Here, the high-frequency fringes of the optical $N00N$ -state are mapped onto the mechanical position probability distribution. Importantly, the states generated by our scheme can exhibit strong negativity of the Wigner quasi-probability distribution independent of the optomechanical coupling strength μ . As shown in Fig. 4C, this negativity approaches zero from below asymptotically with increasing \bar{n} thus the scheme is resilient against initial thermal occupation. Furthermore, we would like to highlight that when using large $N00N$ states this negativity scales with \bar{n}^{-1} . This scaling should be contrasted to the scaling available using single quanta addition [34], which goes with \bar{n}^{-2} , see the supplementary for more details. Moreover, for low amplitude optical coherent states, our scheme is robust against optical loss and inefficiency due to the single photon conditioning.

DISCUSSION

We have introduced a technique that exploits the quantum nature of multi-photon measurements to generate non-classical states of motion of a mechanical resonator. Additionally, we have performed a proof-of-concept experimental demonstration of this technique, which allowed for the first observation of mechanical interference fringes within a thermal distribution. These fringes, albeit at a classical level, have the same qualitative form as those expected from a canonical quantum superposition state, which would be the result of applying our method to a low entropy initial state. This highlights that the appearance of fringes in the position quadrature distribution is not a sufficient condition for non-classical behaviour. Moreover, fringes can be generated by our method independent of the initial thermal occupation, which emphasizes the importance of precise calibration of the position quadrature measurements and characterization of the initial state. While our continuous-wave read-out technique is suitable for the regime experimentally tested here, this technique cannot resolve displacements below the size of the ground state, which is required to observe mechanical non-classicality. Different techniques, such as quantum non-demolition pulsed quadrature measurements [23, 37] will allow this limit to be surpassed and perform mechanical quantum state recon-

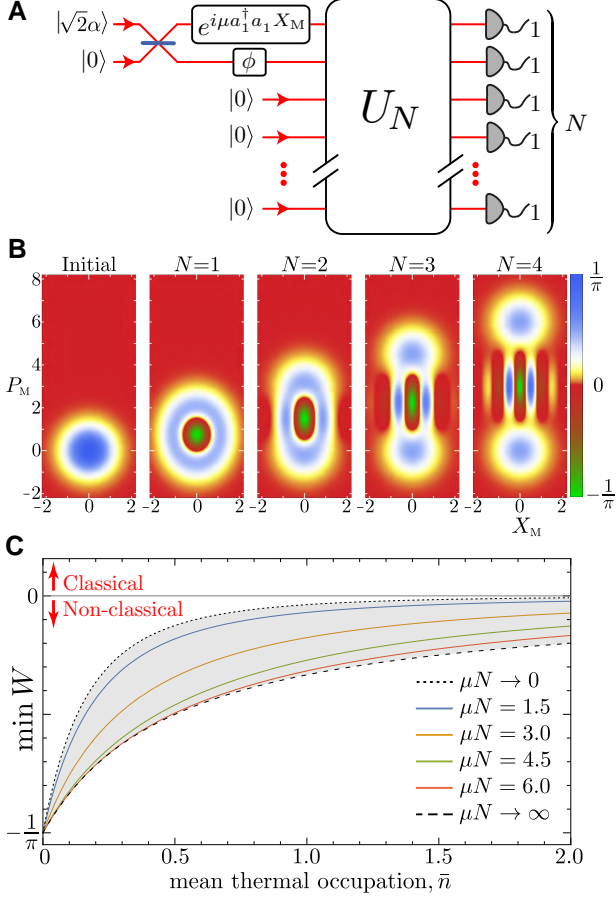


FIG. 4. Generation of larger superposition states. (A) Optical setup requiring two input coherent states, a linear optical network U_N , and single photon counters. One of the two input coherent states interacts with the mechanical resonator and then the inputs are projected onto an optical $N00N$ state, which generates a mechanical superposition state with a separation that increases with N , see text. (B) Simulated Wigner functions for an initial mechanical ground state ($\bar{n} = 0$) and superposition states prepared via multi-photon detection. From left to right: initial ground state, and mechanical states prepared using 1-, 2-, 3-, 4-photon $N00N$ -state projections for $\mu = 1.5$ and $\phi = 0$. Note that these mechanical states are generated via superposition of identity and displacement and are thus not symmetric around the origin. (C) Minimum of the Wigner distribution ($\min W$) as a function of the initial thermal occupation \bar{n} for various values of μN . Note that our scheme generates Wigner-negativity even in the limit of weak coupling $\mu N \rightarrow 0$ (dotted, black line) and saturates for large coupling $\mu N \rightarrow \infty$ (dashed, black line). All experimental configurations (i.e. arbitrary values of μ , N and \bar{n}) result in states within the grey shaded area, and always feature Wigner-negativity. Moreover, for arbitrary single-photon coupling strength μ and arbitrary $N00N$ -state size N the generated states achieve the maximum possible negativity of $-1/\pi$, as $\bar{n} \rightarrow 0$. The coloured solid lines correspond to $N = 1, 2, 3, 4$ multi-photon coincidence events, for $\mu = 1.5$, as in Fig.B.

struction [38]. Looking ahead, one possible experimental approach to generating significant non-classicality with our scheme is to use MHz-frequency oscillators, which have been experimentally cooled to a thermal occupation of $\bar{n} \simeq 0.34$ [39]. For electro-mechanical systems, one could employ a secondary coupling outside the resolved-sideband regime to a weak optical field or to a microwave field together with superconducting qubits, to implement our protocol. At this thermal occupation, the Wigner negativity generated by our scheme for weak coupling is -0.07 , and in the limit of strong coupling is -0.19 , which should be compared with the maximum value achievable of $-\pi^{-1} \simeq -0.32$.

Our scheme offers four main advantages: (i) Our process generates non-classical mechanical states—signified by negativity in the Wigner quasiprobability distribution—without the need for strong single photon coupling and (ii) with favourable scaling against the initial thermal occupation. (iii) Our scheme is resilient against optical loss, as photon counting with low amplitude input coherent states can be used. And (iv), larger superposition states can be prepared by changing only the measurement and projecting onto optical $N00N$ states. This combination of advantages thus dramatically improves the feasibility to generate and observe mechanical single-mode non-classicality—a key outstanding goal of the field—and the high-visibility mechanical fringes observed here are a key step towards achieving this goal.

ACKNOWLEDGMENTS

We would like to thank C. M. Caves, M. S. Kim, G. J. Milburn, I. Pikovski, J. Schmiedmeyer, and F. Shahandeh for helpful discussions and B. Duffus and T. Vulpecula for experimental assistance. This work was supported by an ARC Discovery Project (DP140101638) and in part by the ARC Centres for Engineered Quantum Systems (CE110001013) and Quantum Computation and Communication Technology (CE110001027). AGW acknowledges support through a UQ Vice-Chancellor's Research and Teaching Fellowship, and MRV through a UQ Early Career Researcher Grant.

Supplementary Information: Generation of Mechanical Interference Fringes by Multi-Photon Quantum Measurement

Here we provide further details of the theoretical model, the experimental setup, and the data analysis techniques used.

SI. THEORETICAL MODEL

In this section we give a mathematical model to describe mechanical state preparation via interaction with an optical field followed by photon counting as introduced in this work. We first discuss the details of the two-port case, which can be achieved using a standard Mach-Zehnder interferometer configuration. We then generalise this to multi-port interferometry, which can be used to generate larger mechanical superposition states by projection onto an optical $N00N$ state.

A. Two-port model

For optomechanical systems where the interaction time is much shorter than the mechanical period the mechanical free evolution can be neglected, and the radiation-pressure interaction is in this case described by the unitary

$$U = e^{i\mu a_1^\dagger a_1 X_M}. \quad (S1)$$

Here, a_1 is optical annihilation operator in mode 1 ($[a_1, a_1^\dagger] = 1$), and $X_M = (b + b^\dagger)/\sqrt{2}$ is the mechanical position operator in units of the mechanical quantum noise for mechanical annihilation operator b . Defining $X_M = x/x_0$, and $P_M = p/p_0$ (with mechanical position x , and momentum p), we have $[X_M, P_M] = i$ for $[x, p] = i\hbar$ and $x_0 = \sqrt{\hbar/(m\omega_M)}$ and $p_0 = \sqrt{\hbar m\omega_M}$ where m is the effective mass and ω_M is the mechanical angular frequency. The unitary in Eq. (S1) accurately describes our cavity-free experiment, which uses a simple reflection, as well as cavity-based experiments in the regime where the cavity amplitude decay rate κ is much larger than the mechanical resonance frequency.

The optomechanical coupling strength, μ , quantifies the momentum kick per photon in units of p_0 . For the simple case of a single reflection this strength is

$$\mu = 4\pi x_0/\lambda, \quad (S2)$$

where λ is the optical wavelength. This can easily be seen by noting that: (i) the momentum transfer per single photon $p_0\mu = 2\hbar k = 4\pi\hbar/\lambda$, and (ii) that phase shift $\mu X_M = 2kx$, where k is the optical wavenumber. For a cavity-optomechanical system with interaction Hamiltonian $H/\hbar = -g_0 a_1^\dagger a_1 (b + b^\dagger)$ the momentum kick per photon is enhanced linearly by the cavity finesse \mathcal{F}

$$\mu \propto \frac{g_0}{\kappa} = \frac{4\mathcal{F}x_0}{\lambda}. \quad (S3)$$

We will use a Kraus operator approach to determine the state of the mechanical resonator conditioned on a ‘click’-event in the interferometer. The Kraus- or measurement operator also allows the heralding probabilities for these events to be easily computed.

For our two-port case, the Kraus operator is

$$\Upsilon_{m,n} = {}_2\langle n| {}_1\langle m| B_{12} e^{i\mu a_1^\dagger a_1 X_M} |\alpha\rangle_1 |\alpha e^{i\phi}\rangle_2, \quad (S4)$$

where $\alpha \in \mathbb{R}$ denotes the coherent-state size, B_{12} is the beam-splitter operator, and we have included the static phase shift ϕ into the coherent state inside the interferometer. Using a matrix representation, we write the action of a 50:50 beam-splitter as

$$\begin{pmatrix} a_1 \\ a_2 \end{pmatrix} \rightarrow \frac{1}{\sqrt{2}} \begin{pmatrix} 1 & 1 \\ 1 & -1 \end{pmatrix} \begin{pmatrix} a_1 \\ a_2 \end{pmatrix}. \quad (S5)$$

The measurement operator then becomes

$$\Upsilon_{m,n} = \frac{e^{-\alpha^2}}{\sqrt{m!n!}} \frac{\alpha^{m+n}}{(\sqrt{2})^{m+n}} (e^{i\mu X_M} + e^{i\phi})^m (e^{i\mu X_M} - e^{i\phi})^n. \quad (S6)$$

The state of the mechanical resonator after the interaction and ‘click’-event is determined by

$$\rho_M^{\text{out}} = \Upsilon \rho_M^{\text{in}} \Upsilon^\dagger / \mathcal{P}, \quad (S7)$$

where \mathcal{P} is the heralding probability, which ensures that $\text{Tr}\{\rho_M^{\text{out}}\} = 1$.

Important to this work is observing the mechanical position probability distribution after the interaction and measurement. The operator Υ depends only on the operator X_M and we can thus write

$$\langle X_M | \rho_M^{\text{out}} | X_M \rangle = \frac{1}{\mathcal{P}} \Upsilon^\dagger(X_M) \Upsilon(X_M) \langle X_M | \rho_M^{\text{in}} | X_M \rangle. \quad (S8)$$

Hence, $\Upsilon^\dagger \Upsilon$ can be interpreted as a filter, acting on the position distribution of the resonator

$$\Upsilon^\dagger \Upsilon = \frac{1}{m!n!} e^{-2\alpha^2} \alpha^{2m} \alpha^{2n} \times (1 + \cos(\mu X_M - \phi))^m (1 - \cos(\mu X_M - \phi))^n. \quad (S9)$$

Note that α will only affect the heralding probability and does not change the form of the conditional mechanical state. See Figs. 2 and 3 of the main text for experimental observations of such mechanical interference fringes. The heralding probability \mathcal{P} is given by

$$\begin{aligned} \mathcal{P} &= \text{Tr}\{\Upsilon^\dagger \Upsilon \rho_M^{\text{in}}\} \\ &= \int_{-\infty}^{\infty} dX_M \Upsilon^\dagger \Upsilon \langle X_M | \rho_M^{\text{in}} | X_M \rangle. \end{aligned} \quad (S10)$$

For a mechanical thermal state with position distribution

$$\langle X_M | \rho_M^{\text{in}} | X_M \rangle = \frac{1}{\sqrt{\pi(1+2\bar{n})}} \exp \left[\frac{-X_M^2}{1+2\bar{n}} \right], \quad (\text{S11})$$

where \bar{n} is the mean thermal occupation, the heralding probabilities $\mathcal{P}_{m,n}$ for the click events $\{m,n\}$ take the form

$$\begin{aligned} \mathcal{P}_{0,0} &= e^{-2\alpha^2}, \\ \mathcal{P}_{0,1} &= e^{-2\alpha^2} \alpha^2 (1 - e^{-\mu^2(1+2\bar{n})/4} \cos \phi), \\ \mathcal{P}_{1,0} &= e^{-2\alpha^2} \alpha^2 (1 + e^{-\mu^2(1+2\bar{n})/4} \cos \phi), \\ \mathcal{P}_{1,1} &= \frac{1}{2} e^{-2\alpha^2} \alpha^4 (1 - e^{-\mu^2(1+2\bar{n})} \cos(2\phi)). \end{aligned} \quad (\text{S12})$$

Note that for finite α and $\mu^2(1+2\bar{n}) > 0$ the heralding probability is non-zero for all ϕ .

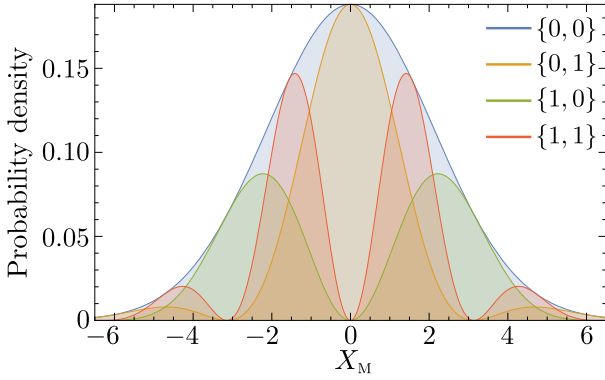


FIG. S1. **Unnormalized theoretical mechanical position probability distributions for various click-events.** An initial Gaussian state ($\{0,0\}$) is subject to $\Upsilon_{m,n}$, with $\mu = 1, \bar{n} = 4, \phi = \pi$ for single-photon ($\{0,1\}, \{1,0\}$) and two-photon ($\{1,1\}$) click-events. Note that the case $\{1,1\}$ generates a fringe-pattern with twice the frequency compared to the single-photon cases.

B. Multi-port model

Here we discuss how larger mechanical superposition states can be generated using single photon detection at each of the outputs of a multi-port interferometer. See Fig. 4A for an optical schematic. A coherent state interacts with a mechanical resonator and then (together with a second reference coherent state) is projected onto an optical $N00N$ state where N is the size of multi-port. The mechanics will have then undergone a superposition of the identity operation (zero photons) and a displacement corresponding to the N -photon radiation pressure kick. The corresponding unitary U_N for a real-bordered symmetric canonical multi-port, can be represented by a matrix with elements

$$M_N^{(k,l)} = \frac{1}{\sqrt{N}} e^{i2\pi kl/N}, \quad (\text{S13})$$

where $k, l \in [0, N-1]$. This form is a multi-port generalisation of the matrix used in Eq. (S5). As an example, the three-port case is

$$\mathbf{M}_3 = \frac{1}{\sqrt{3}} \begin{pmatrix} 1 & 1 & 1 \\ 1 & e^{i2\pi/3} & e^{i4\pi/3} \\ 1 & e^{i4\pi/3} & e^{i2\pi/3} \end{pmatrix}. \quad (\text{S14})$$

The output field operators are given by $a_{\text{out}} = \mathbf{M} a_{\text{in}}$, where $a_{\text{in/out}}$ are N -dimensional column vectors. The state of light before the unitary U_N for an N -fold coincidence event is

$$\begin{aligned} &\langle 000 \dots 0 | a_N \dots a_3 a_2 a_1 U_N^\dagger = \\ &\langle 000 \dots 0 | U_N a_N U_N^\dagger \dots U_N a_3 U_N^\dagger U_N a_2 U_N^\dagger U_N a_1 U_N^\dagger. \end{aligned} \quad (\text{S15})$$

Here $U_N a_j U_N^\dagger$ is readily computed from the matrix expression, Eq. (S13) above.

In our scheme vacuum is injected into modes 3 to N , which leaves an optical $N00N$ state in modes 1 and 2. Vacuum inputs in modes 3 to N implies that only the first two columns of \mathbf{M} (Eq. (S13)) are being used. That is, there is no excitation in modes 3 to N . We can then write the un-normalised state for modes 1 and 2 as

$$\langle \varphi_{1,2} | \propto \langle 00 | \frac{1}{(\sqrt{N})^N} \prod_{m=0}^{N-1} (a_1 + e^{-i2\pi m/N} a_2). \quad (\text{S16})$$

All the cross terms in the product vanish and we have

$$\begin{aligned} \langle \varphi_{1,2} | &\propto \frac{1}{(\sqrt{N})^N} \langle 00 | (a_1^N - (-1)^N a_2^N), \\ &\propto \frac{\sqrt{N}!}{(\sqrt{N})^N} (\langle 0N | - (-1)^N \langle N0 |). \end{aligned} \quad (\text{S17})$$

The measurement operator that acts on the mechanical resonator for this multi-port case is then

$$\Upsilon_N = \frac{1}{(\sqrt{N})^N} e^{-|\alpha|^2} \alpha^N (e^{iN\mu X_M} - (-1)^N e^{iN\phi}). \quad (\text{S18})$$

Choosing $\phi = \pi$ as in the main text, this operator has the same form as $\Upsilon_{1,0}$. The displacements, however, are increased by a factor of N , compared to Eq.(S9). As a consequence, the frequency of the cosine in the filter-function $\Upsilon_N^\dagger \Upsilon_N$ is increased by a factor of N and thus exhibit phase-super resolution.

$$\Upsilon_N^\dagger \Upsilon_N = \frac{2}{N^N} e^{-2|\alpha|^2} |\alpha|^{2N} (1 - (-1)^N \cos(N\mu X_M - N\phi)). \quad (\text{S19})$$

Using this expression we can also compute the heralding probability $\mathcal{P}_N = \text{Tr} \{ \Upsilon_N^\dagger \Upsilon_N \rho_M \}$, which, for an initial thermal state with \bar{n} is given by

$$\begin{aligned} \mathcal{P}_N(\bar{n}) &= \frac{2}{N^N} e^{-2|\alpha|^2} |\alpha|^{2N} \times \\ &(1 - (-1)^N \exp[-\frac{1}{4}\mu^2(1+2\bar{n})N^2] \cos(N\phi)). \end{aligned} \quad (\text{S20})$$

Importantly, this expression is always positive when the mechanical position distribution has non-zero spread, $\mu^2(1 + 2\bar{n}) > 0$.

Using $\Upsilon_N^\dagger \Upsilon_N$ we can quantify how much Wigner-negativity can be generated by our scheme for given parameters N , \bar{n} and μ . We find that the minimum of the Wigner-function is given by

$$\min W = \frac{-1}{\pi(1 + 2\bar{n})} \frac{1 - \exp[-(1/4)\mu^2 N^2/(1 + 2\bar{n})]}{1 - \exp[-(1/4)\mu^2 N^2(1 + 2\bar{n})]}. \quad (\text{S21})$$

Note that for $\bar{n} = 0$, $\min W = -1/\pi$ independent of the other parameters, reaching the lowest possible value for a Wigner function. In the opposite limit, where $\bar{n} \rightarrow \infty$, $\min W$ approaches zero from below, see Fig. S2A. Note also, that projecting onto larger optical $N00N$ -states increases the generated Wigner-negativity for fixed thermal occupation \bar{n} , as illustrated in Fig. S2B.

It is also instructive to study the limits of weak ($\mu N \rightarrow 0$) and strong ($\mu N \rightarrow \infty$) optomechanical coupling

$$\min W \xrightarrow{\mu N \rightarrow 0} \frac{-1}{\pi} \frac{1}{(1 + 2\bar{n})^3}, \quad (\text{S22})$$

$$\min W \xrightarrow{\mu N \rightarrow \infty} \frac{-1}{\pi} \frac{1}{1 + 2\bar{n}}. \quad (\text{S23})$$

Thus, Wigner negativity is generated by our scheme even for weak optomechanical coupling. Moreover, the amount of negativity that can be generated is bounded by the two power-laws Eqs. (S22),(S23), as shown in Fig. 4C and Fig. S2A

SII. EXPERIMENTAL DETAILS

Our experiment makes use of an inherently stable polarization interferometer design, which can be intuitively understood in analogy to a Mach-Zehnder interferometer (MZI), see Fig. S3. The interferometer has two modes, which are represented by orthogonal polarizations $|H\rangle$ and $|V\rangle$. A half-wave plate takes the role of the beam splitter in the MZI, with the advantage of a very precise and continuously tunable splitting ratio. The two polarization modes are then separated into different spatial modes for the interaction with the mechanical resonator and recombined afterwards, using calcite beam displacers. This design achieves good phase stability due to common-mode rejection of all non-rotational mechanical noise, without requiring any active locking.

With our implementation the two beam splitters in the MZI are the same optical element and thus constrained to equal splitting ratios, which, however, is not a restriction for our experiment. Furthermore, our experimental arrangement allows to probe the position of the membrane from the other side, which significantly simplifies the experimental setup. Independent of losses in the setup, the optimal signal-to-noise ratio (SNR) is achieved with a splitting ratio of $1/2$.

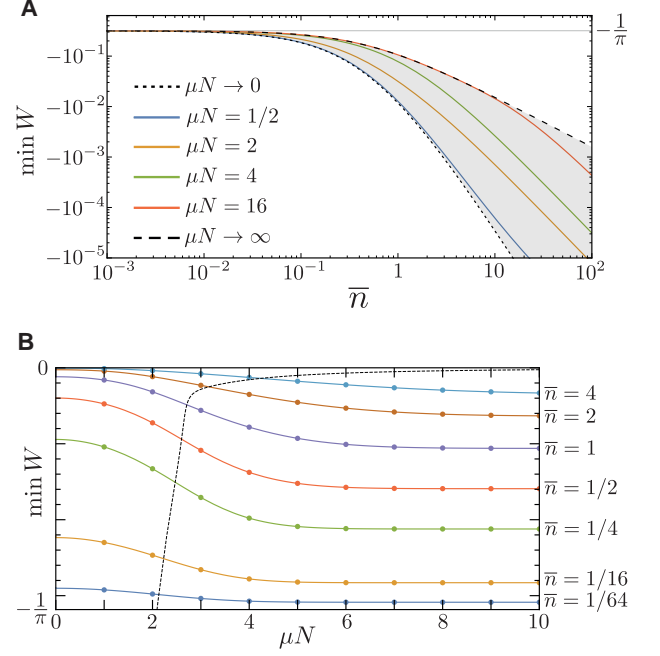


FIG. S2. **Wigner-negativity generated by our scheme.** (A) Loglog-plot of the Wigner-negativity as a function of the initial thermal occupation for various values of μN . For small \bar{n} the generated negativity is close to the maximal value of $-1/\pi$, and experiences power-law behaviour for large \bar{n} . (B) Wigner-negativity as a function of μN for various values of initial thermal occupation \bar{n} . The black-dashed line traces the inflection-points of the negativity as a function of μN and is given to aid observation of the scaling of these curves.

In order to achieve a large initial thermal state, the membrane was mounted on a Steminc SM412 ring-piezo with a capacitance of 1.8 nF and a nominal resonance frequency of 1.7 MHz. The piezo was driven with noise across the mechanical resonance frequency at 106 kHz. Note, however, that the drive couples to $\sqrt{X^2 + P^2}$, such that the drive voltage must be Chi-distributed in order to achieve Gaussian initial states in X and P . The piezo was driven with a discretized version of this distribution, sampled at 3.2 MS/s. Figure S4 shows this distribution, together with the measured distributions of X , P and $\sqrt{X^2 + P^2}$.

Synchronization of the two APDs for coincidence detection and of the APDs and the balanced detector for the position measurement was achieved using a pulsed laser diode. The diode pulses with a FWHM of 12 ns at a variable repetition rate were used as an input on the position readout side. The beam was reflected off the membrane and detected by the balanced photodetector, with one input blocked. Part of the beam is transmitted through the membrane, attenuated to the single-photon level and detected by the APDs. This technique allowed for synchronization of the two APDs to within 1 ns and between single-photon detection and position readout to within 7 ns, which is 4 orders of magnitude below the

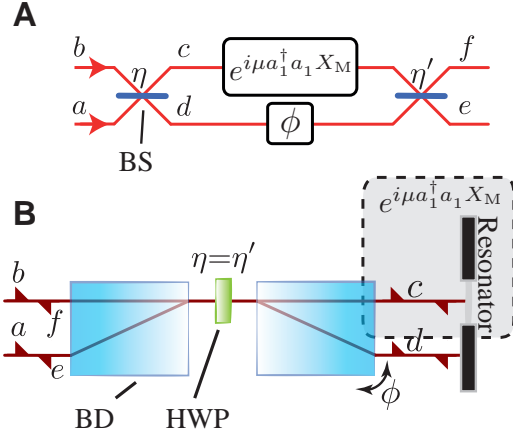


FIG. S3. **Reflective polarization Mach-Zehnder interferometer.** (A) In a standard Mach-Zehnder interferometer, an input beam in mode a or b is split on a beamsplitter (BS) with reflectivity r_p into two spatial modes c and d . One mode obtains a static phase-shift ϕ , while the other interacts with the mechanical resonator via $e^{i\mu a_1^\dagger a_1 X_M}$. The two beams then interfere on a second beamsplitter with reflectivity r_p' and are split into the output modes e and f . (B) In the polarization interferometer the modes a, d, e correspond to horizontal polarization and b, c, f to vertical polarization. The BS are replaced by a half-waveplate (HWP), which allows for precise control of the splitting ratio. In the reflective design here, the polarization modes are spatially separated on a calcite beamdisplacer (BD). One of the beams reflects off the mechanical resonator, the other of the static frame of the resonator. The beams are recombined into the same spatial mode and interfere in the HWP. Finally they can be separated using another BD. The arrow over the mode-labels indicates the propagation direction.

time of a mechanical period.

III. DATA ANALYSIS

Upon an appropriate trigger signal (either APD1-click, APD2-click or coincidence click within 7.8 ns) a trace of the homodyne signal is recorded. This trace consists of 5000 points, sampled at a rate of 100 MS/s, thus resulting in a window of $\pm 25\mu\text{s}$ around the trigger event. The X - and P -values for each trace were obtained from a fit of the mechanical response function and the phase-space distribution was reconstructed from 3000 such measurements. The expected mechanical response function is of the form

$$A * \cos(X \cos[\omega_M t] + P \sin[\omega_M t] + \phi_R) + c, \quad (\text{S24})$$

where A is the full amplitude of the homodyne signal, ω_M is the mechanical resonance frequency, ϕ_R is the static phase of the readout interferometer and c is the residual DC-component in the signal due to asymmetric loss in the two arms of the homodyne interferometer. In our experiment we used a balanced photodetector with a gain

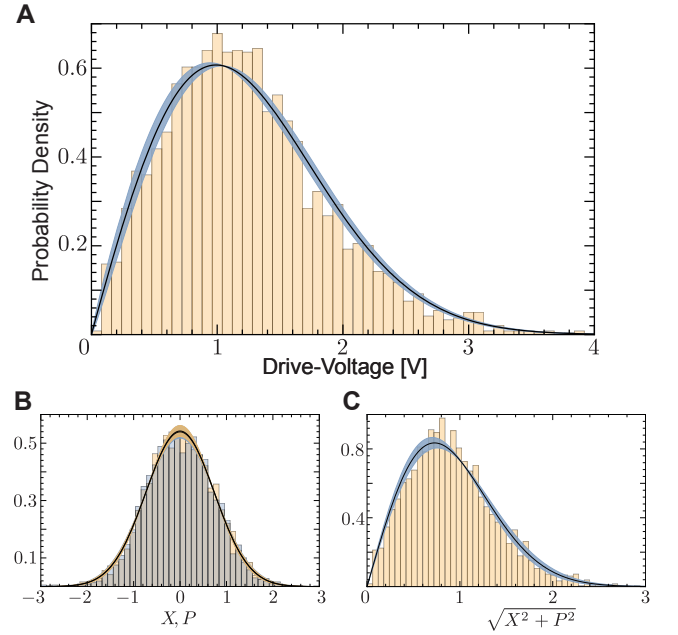


FIG. S4. **Drive spectrum and response of the mechanical resonator.** (A) Probability density histogram of the measured voltage distribution used to drive the piezo. The orange line corresponds to a Chi-distribution fit with shape-parameter $\nu = 1.98 \pm 0.03$ and the blue shaded area represents the 3σ confidence region of the fit. (B) The measured distributions of X (blue) and P (orange) using the drive in Fig. A, together with fitted Normal-distributions (blue and orange lines, respectively) with shape-parameters $\sigma_x = 0.740 \pm 0.009$ and $\sigma_p = 0.735 \pm 0.008$, respectively. The corresponding 3σ confidence regions are shown in complementary colors (orange and blue, respectively). (C) The phase-space norm $\sqrt{X^2 + P^2}$ is linearly proportional to the drive-voltage and is thus well-described by a Rayleigh distribution with shape-parameter $\sigma = 0.727 \pm 0.008$ (solid line with shaded 3σ regions).

of 10^5 V/A and a bandwidth of 4 MHz, and the DC-component c was compensated to zero by adding a tunable loss element in front of one detector. Since ω_M , A and c were measured independently and remained constant throughout the experiment, the only free variables in the fit were X , P and the read-out phase ϕ_R . These variables have distinct effects on the shape of the response, thus allowing for unique and stable fitting.

While Eq. (S24) describes the response very well in the low drive regime $\sqrt{X^2 + P^2} \lesssim 1$, we observe a mechanical position dependent optical amplitude modulation in the readout signal for larger drive. We attribute this amplitude modulation to a mechanical position dependent change in the reflectivity which is consistent with additional measurements of the optical transmission with time. The reflectivity of the mechanical device is dependent on thin-film interference and thus any small change in the refractive index of the can significantly affect the reflectivity. We modelled this modulation using a multi-

plicative function of the form

$$1 - d * \left| \cos \left[\omega_M t + \arctan(X/P) - \frac{\pi}{4} \right] \right|, \quad (\text{S25})$$

where d describes the relative strength of the amplitude modulation. The parameter d was used as an additional free parameter in the fit and was found to scale linearly with the drive strength. We used the function $1 - d|x|$ as the first-order approximation, which gave stable fits in the regime used. The arctan term transforms to the rotating-frame picture, while the $\pi/4$ phase-shift results in zero modulation when the membrane position is zero.

Note that the absolute value implies that the modulation depends on the displacement of the membrane, but not the direction. This model describes the observed response very well for $\sqrt{X^2 + P^2} \lesssim 3.2$, which is the regime where all data was taken. For larger drive we observe an additional asymmetry in the amplitude modulation that might be due to anisotropic stress in the material. Finally, for very low drive strength, the signal-to-noise ratio is limited by the resolution of the oscilloscope, resulting in a truncation in the center of the phase-space plot in Fig. 2A.

-
- [1] C. J. Davisson, L. H. Germer, *Nature* **119**, 558-560 (1927).
 - [2] H. Rauch, W. Treimer, U. Bonse, *Phys. Lett. A* **47**, 369–371 (1974).
 - [3] C. Monroe, D. M. Meekhof, B. E. King, D. J. Wineland, *Science* **272**, 1131–1136 (1996).
 - [4] Y. Shin, M. Saba, T. A. Pasquini, W. Ketterle, D. E. Pritchard, A. E. Leanhardt, *Phys. Rev. Lett.* **92**, 050405 (1992).
 - [5] S. Eibenberger, S. Gerlich, M. Arndt, M. Mayor, J. Tuxen, *Phys. Chem. Chem. Phys.* **15**, 14696–14700 (2013).
 - [6] M. Aspelmeyer, T. J. Kippenberg, F. Marquardt, *Rev. Mod. Phys.* **86**, 1391–1452 (2014).
 - [7] S. Bose, K. Jacobs, P. Knight, *Phys. Rev. A* **59**, 3204–3210 (1999).
 - [8] W. Marshall, C. Simon, R. Penrose, D. Bouwmeester, *Phys. Rev. Lett.* **91**, 130401 (2003).
 - [9] I. Pikovski, M. R. Vanner, M. Aspelmeyer, M. S. Kim, C. Brukner, *Nature Physics* **8**, 393–397 (2012).
 - [10] R. W. Andrews, *et al.* *Nature Physics* **10**, 321–326 (2014).
 - [11] D. Rugar, R. Budakian, H. J. Mamin, B. W. Chui, *Nature* **430**, 329–332 (2004).
 - [12] C. M. Caves, *Phys. Rev. D* **23**, 1693–1708 (1981).
 - [13] LIGO Scientific Collaboration and Virgo Collaboration, *Phys. Rev. Lett.* **116**, 061102 (2016).
 - [14] A. D. O’Connell, *et al.* *Nature* **464**, 697–703 (2010).
 - [15] K. C. Lee, *et al.* *Nature Photonics* **6**, 41–44 (2012).
 - [16] M. R. Vanner, M. Aspelmeyer, and M. S. Kim, *Phys. Rev. Lett.* **110**, 010504 (2013).
 - [17] R. Riedinger, *et al.* *Nature* **530**, 313–316 (2016).
 - [18] E. Verhagen, *et al.* *Nature* **482**, 63–67 (2012).
 - [19] T. P. Purdy, P. L. Yu, R. W. Peterson, N. S. Kampel, C. A. Regal, *Phys. Rev. X* **3**, 031012 (2013).
 - [20] A. Safavi-Naeini, *et al.* *Nature* **500**, 185–189 (2013).
 - [21] T. A. Palomaki, J. D. Teufel, R. W. Simmonds, K. W. Lehnert, *Science* **342**, 710–713 (2013).
 - [22] E. Knill, R. Laflamme, and G. J. Milburn, *Nature* **409**, 46–52 (2001).
 - [23] M. R. Vanner, *et al.* *Proc. Natl. Acad. Sci. USA* **108**, 16182–16187 (2011).
 - [24] A. N. Boto, *et al.* *Phys. Rev. Lett.* **85**, 2733 (2000).
 - [25] P. Walther, *et al.*, *Nature* **429**, 158 (2004).
 - [26] M. W. Mitchell, J. S. Lundeen, A. M. Steinberg, *Nature* **429**, 161 (2004).
 - [27] K. J. Resch, *et al.* *Phys. Rev. Lett.* **98**, 223601 (2007).
 - [28] G. C. Ghirardi, A. Rimini, T. Weber, *Phys. Rev. D* **34**, 470–491 (1986).
 - [29] L. Diosi, *Phys. Rev. A* **40**, 1165–1174 (1989).
 - [30] R. Penrose, *Gen. Relat. Gravit.* **28**, 581–600 (1996).
 - [31] G. Khoury, H. S. Eisenberg, E. J. S. Fonseca, D. Bouwmeester, *Phys. Rev. Lett.* **96**, 203601 (2006).
 - [32] A. B. Zwickl, *et al.* *Appl. Phys. Lett.* **92**, 103125 (2008).
 - [33] M. Ringbauer, B. Duffus, C. Branciard, E. G. Cavalcanti, A. G. White, A. Fedrizzi, *Nature Physics* **11**, 249–254 (2013).
 - [34] A. Zavatta, V. Parigi, M. Bellini, *Phys. Rev. A* **75**, 052106 (2007).
 - [35] D. Kleckner, I. Pikovski, *et al.* *New J. Phys.* **10**, 095020 (2008).
 - [36] B. Pepper, R. Ghobadi, E. Jeffrey, C. Simon, D. Bouwmeester, *Phys. Rev. Lett.* **109**, 023601 (2012).
 - [37] M. R. Vanner, J. Hofer, G. D. Cole, M. Aspelmeyer, *Nat. Commun.* **4**, 2295 (2013).
 - [38] M. R. Vanner, I. Pikovski, M. S. Kim, *Ann. Phys. (Berlin)* **527**, 15–26 (2015).
 - [39] J. D. Teufel, *et al.* *Nature* **475**, 359–363 (2011).